Science Advances
AAAS

advances.sciencemag.org/cgi/content/full/6/16/eaaz4261/DC1

Supplementary Materials for

Three-dimensional vectorial holography based on machine learning inverse design

Haoran Ren, Wei Shao, Yi Li, Flora Salim, Min Gu*

*Corresponding author. Email: gumin@usst.edu.cn

Published 17 April 2020, *Sci. Adv.* **6**, eaaz4261 (2020)
DOI: 10.1126/sciadv.aaz4261

The PDF file includes:

Other Supplementary Material for this manuscript includes the following:

(available at advances.sciencemag.org/cgi/content/full/6/16/eaaz4261/DC1)

Supplementary Notes

Note S1. Vectorial diffraction theory under the Helmholtz condition

According to the vectorial Debye theory, a vectorial electric field in a homogeneous dielectric medium close to the focus can be described by[29]

$$\mathbf{E}(x,y,z) = -\frac{if}{\lambda k_t^2}\iint_{r\le R}(\mathbf{E}_t(\theta,\phi)e^{ik_z z}/\cos\theta)e^{-i(k_x x+k_y y)}dk_x dk_y \tag{S1}$$

which allows to rewrite the Debye diffraction integral as the Fourier transform (FT) of a weighted electric field $\mathbf{E}_t(\theta,\phi)$ as

$$\mathbf{E}(x,y,z) = -\frac{if}{\lambda k_t^2}\Im_{x,y}(\mathbf{E}_t(\theta,\phi)e^{ik_z z}/\cos\theta) \tag{S2}$$

where f is the focal length of a focusing lens (in this paper f is the focal length of a large-angle FT holographic lens), λ is the incident wavelength. $k_t = n_t * k_0$, where n_t is the refractive index of the medium upon the which the light is focused (in this paper n_t=1) and k_0 is the free-space wavenumber. Due to the fact that the wavefront leaving the vectorial hologram features a broad angular spectrum and transforms onto the vectorially weighted Ewald sphere, with the transmitted electric field given as $\mathbf{E}_t(\theta,\phi) = P(\theta)\mathbf{T}(\theta,\phi)\mathbf{E}_{in}$, which includes an apodization factor of $P(\theta)$ and a polarization transformation matrix $\mathbf{T}(\theta,\phi)$ resulting from the depolarization effect. For holographic applications, the Helmholtz condition is used to accommodate 3D uniform imaging that is required in 3D holography, as such the apodization function is given as $P(\theta) = P(r)(\frac{1}{\sqrt{\cos\theta}})^3$ (*31*). To fully consider the depolarization effect on a vectorially weighted Ewald sphere, the polarization transformation matrix $\mathbf{T}(\theta,\phi)$ is given as

$$\mathbf{T}(\theta,\phi)=\begin{bmatrix} 1+(\cos\theta-1)\cos^2\phi & (\cos\theta-1)\cos\phi\sin\phi & -\sin\theta\cos\phi \\ (\cos\theta-1)\cos\phi\sin\phi & 1+(\cos\theta-1)\sin^2\phi & -\sin\theta\cos\phi \\ \sin\theta\cos\phi & \sin\theta\sin\phi & \cos\theta \end{bmatrix} \quad \text{(S3)}$$

which opens the possibility of fully considering an arbitrary 2D vector field with a spatially variant vector distribution.

As explicitly given in Fig. 2B, our machine-learning algorithm predicts that the three azimuthal and radial spatial components can be used to independently manipulate the three orthogonal components (E_x, E_y, E_z) of a 3D vectorial field in the image space. Based on our machine-learning inverse design algorithm, we show that the azimuthal spatial components with the phase modulation of V_{ax} and V_{ay}, which represents a horizontal and vertical π-phase-step, respectively, could be used to control the transverse electric field components E_{x} and E_{y} in the image space, respectively. On the other hand, the radial spatial component could be used to manipulate the longitudinal electric field component E_{z} in the image space. As a result, any incident 2D vector field $\mathbf{E}_{in}$ could be synthesized based on the above azimuthal and radial spatial components:

$$\mathbf{E}_{in}=\begin{bmatrix} E_{inx} \\ E_{iny} \\ E_{inz} \end{bmatrix}=\begin{bmatrix} E_{ax}(-\sin(\phi))\mathrm{e}^{i\phi_{ax}}\,\mathrm{e}^{iV_{ax}}+E_{ay}(-\sin(\phi))\mathrm{e}^{i\phi_{ay}}\,\mathrm{e}^{iV_{ay}}+E_r\cos(\phi)\mathrm{e}^{i\phi_r} \\ E_{ax}\cdot\cos(\phi)\mathrm{e}^{i\phi_{ax}}\,\mathrm{e}^{iV_{ax}}+E_{ay}\cdot\cos(\phi)\mathrm{e}^{i\phi_{ay}}\,\mathrm{e}^{iV_{ay}}+E_r\sin(\phi)\mathrm{e}^{i\phi_r} \\ 0 \end{bmatrix} \quad \text{(S4)}$$

where (E_{ax}, ϕ_{ax}, E_{ay}, ϕ_{ay}, E_{r}, ϕ_{r}) are the MANN-derived amplitude and phase elements. Based on Eq. S4, we can transform the MANN-derived single vector output containing six elements into a 2D vector field, as presented in Fig. 2C and fig. S3.

To investigate the 3D vectorial field distribution at off-axis positions in the image plane, the incident electric field in Eq. S4 was further modified. To this purpose, the correlation between the deflection angle of an optical beam induced by a blazed grating in the hologram plane and the associated spatial shift in the image plane was numerically characterized (figs. S11 A and B). Such angle-dependent diffracted beams could modify the vectorial distribution on the vectorially weighted Ewald sphere. Therefore, the incident vectorial distribution in Eq. S4 should be modified:

$$\mathbf{E}_{in} = \begin{bmatrix} \cos\alpha_x \cdot E_{inx} \\ \cos\alpha_y \cdot E_{iny} \\ \sin\alpha_x \cdot E_{inx} + \sin\alpha_y \cdot E_{iny} \end{bmatrix} \tag{S5}$$

where α_x and α_y denote the deflection angle in the *x* and *y* direction, respectively.

Note S2. Characterization of the diffraction efficiency and viewing angle of a vectorial hologram

The diffraction efficiency of a vectorial hologram was experimentally characterized by moving the laser-printed digital phase hologram into and out of the incident 2D vector beam. As such, the absolute diffraction efficiency was measured as the ratio between the total intensity of the holographic image and that of the same sample area without the digital phase hologram. Furthermore, we show the characterization of the maximal viewing angle of a vectorial hologram. Firstly, the maximal diffraction angle of a digital phase hologram is given as $\beta_{\max} = \tan^{-1}(\lambda / p)$, where λ is the wavelength of light and p is the single pixel size of the hologram which is 0.5 μm in our laser-printed high-resolution hologram. As such, a maximal diffraction angle of 57.9 degree was numerically obtained. Secondly, due to the fact that a large-

angle FT holographic lens with NA=0.8 was embedded in the digital phase hologram, the maximal diffraction angle for the reconstructed holographic image is given as $\beta_{FT} = \sin^{-1}(\mathrm{NA}/n)$, where n is the refractive index of the image media (in this paper n=1). Through a simple mathematical derivation, the maximal holographic image size is linearly scaled by the vectorial hologram size through the relationship of $D_{\mathrm{Im}} = D_{\mathrm{Holo}}\left[\frac{\tan(\beta_{\max}) - \tan(\beta_{FT})}{\tan(\beta_{FT})}\right]$, where D_{Im} and D_{Holo} represent the size of a holographic image and of a vectorial hologram, respectively. For our laser-printed high-resolution vectorial hologram, this relationship is explicitly given as D_{Im}=0.2D_{Holo}. As a result, the viewing angle of a 3D vectorial holographic image is determined by $\vartheta = 2\tan^{-1}\left[(D_{Holo} - D_{\mathrm{Im}})/2f_2\right]$, where f_2 is the reconstruction distance of holographic image, suggesting a significantly enlarged viewing angle of 93.67 degree in our paper, opening the possibility of floating display.

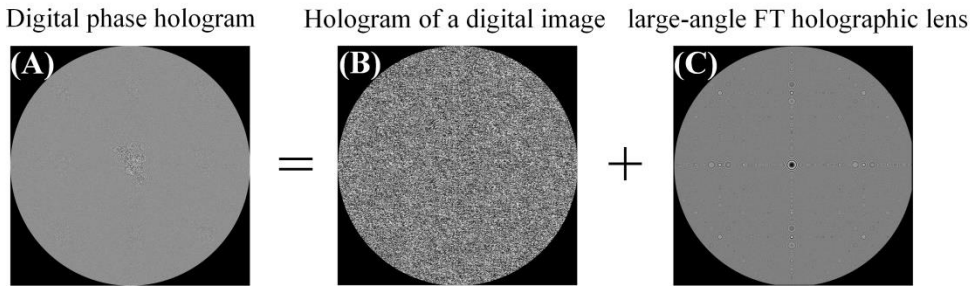

Fig. S1. A digital phase hologram (A) which represents the phase function of a vectorial hologram is superposed by a hologram of a digital image (B) and a large-angle FT holographic lens (C).

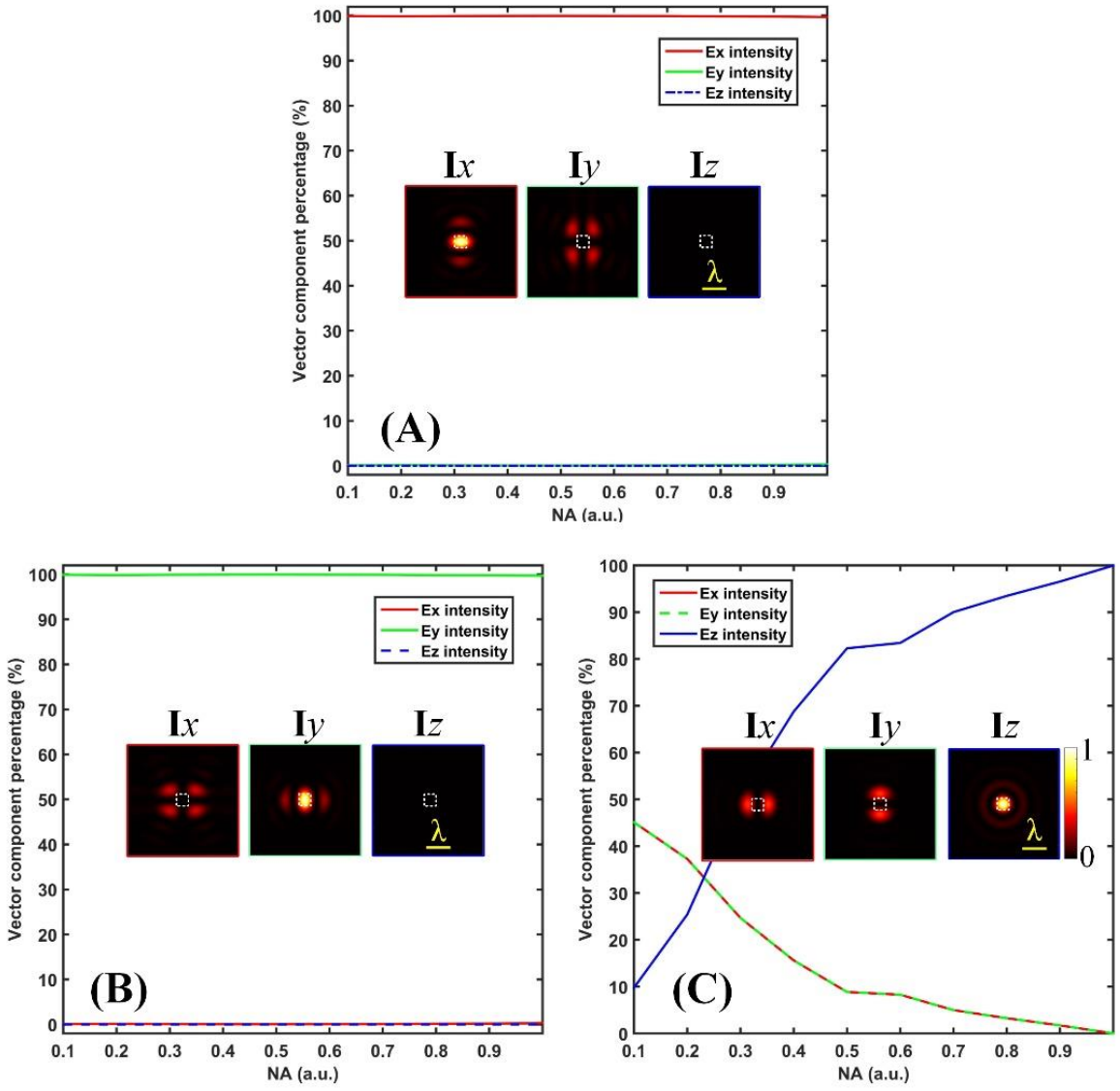

Fig. S2. The strong correlation between the azimuthal and radial spatial components in the hologram plane and the three orthogonal components in the image plane. (**A-C**) The numerically simulated intensity distributions of the three orthogonal components of E_x, E_y, and E_z for different NAs based on the three azimuthal and radial spatial components presented in Fig. 2B, respectively.

(A)

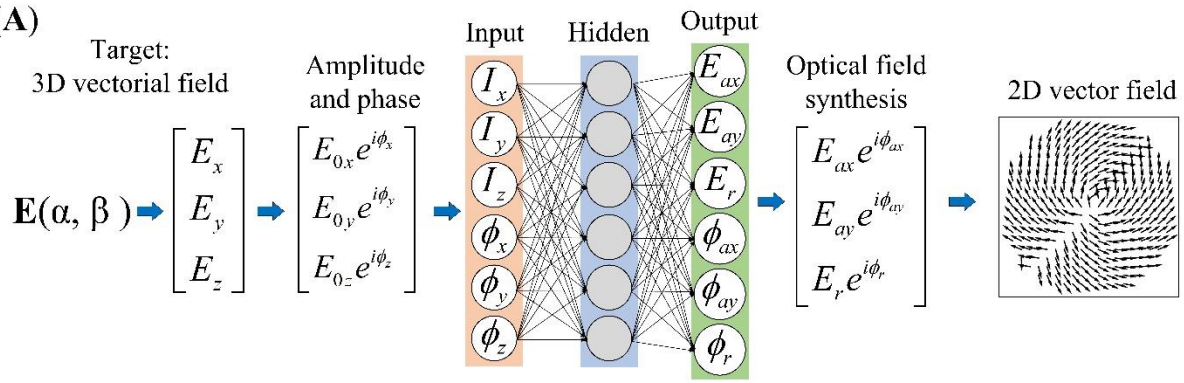

(B)

Targets **E**(α, β)	**E**(0, π/4)	**E**(0, 0)	**E**(π/2, π/4)	**E**(π/4, π/2)	**E**(π/4, π/4)	**E**(3π/4, π/4)
E_{0x}	1/√2	0	0	1/√2	1/√3	1/√3
E_{0y}	0	0	1/√2	1/√2	1/√3	1/√3
E_{0z}	1/√2	1	1/√2	0	1/√3	1/√3
$Ø_x$	0	0	0	0	0	π
$Ø_y$	0	0	0	0	0	0
$Ø_z$	0	0	0	0	0	0
MANNs predictions						
E_{ax}	0.518	0.003	0.008	0.531	0.344	0.326
E_{ay}	0.012	0.003	0.539	0.539	0.368	0.369
E_r	0.538	0.979	0.544	0.009	0.368	0.382
$Ø_{ax}$	0.427	0.436	0.428	0.453	0.429	0.929
$Ø_{ay}$	1.011	1.005	1.010	0.995	0.978	0.940
$Ø_r$	0.469	0.457	0.478	0.456	0.470	0.465
2D vector field		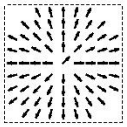				

Fig. S3. The schematic illustration of the MANN model. (**A**) The MANN consists of an input layer specified by the user as an arbitrary 3D vectorial field, a hidden perception layer, and an output layer used for the synthesis of a 2D vector field, respectively. (**B**) MANN-derived 2D vector fields based on any desired 3D vectorial field targets.

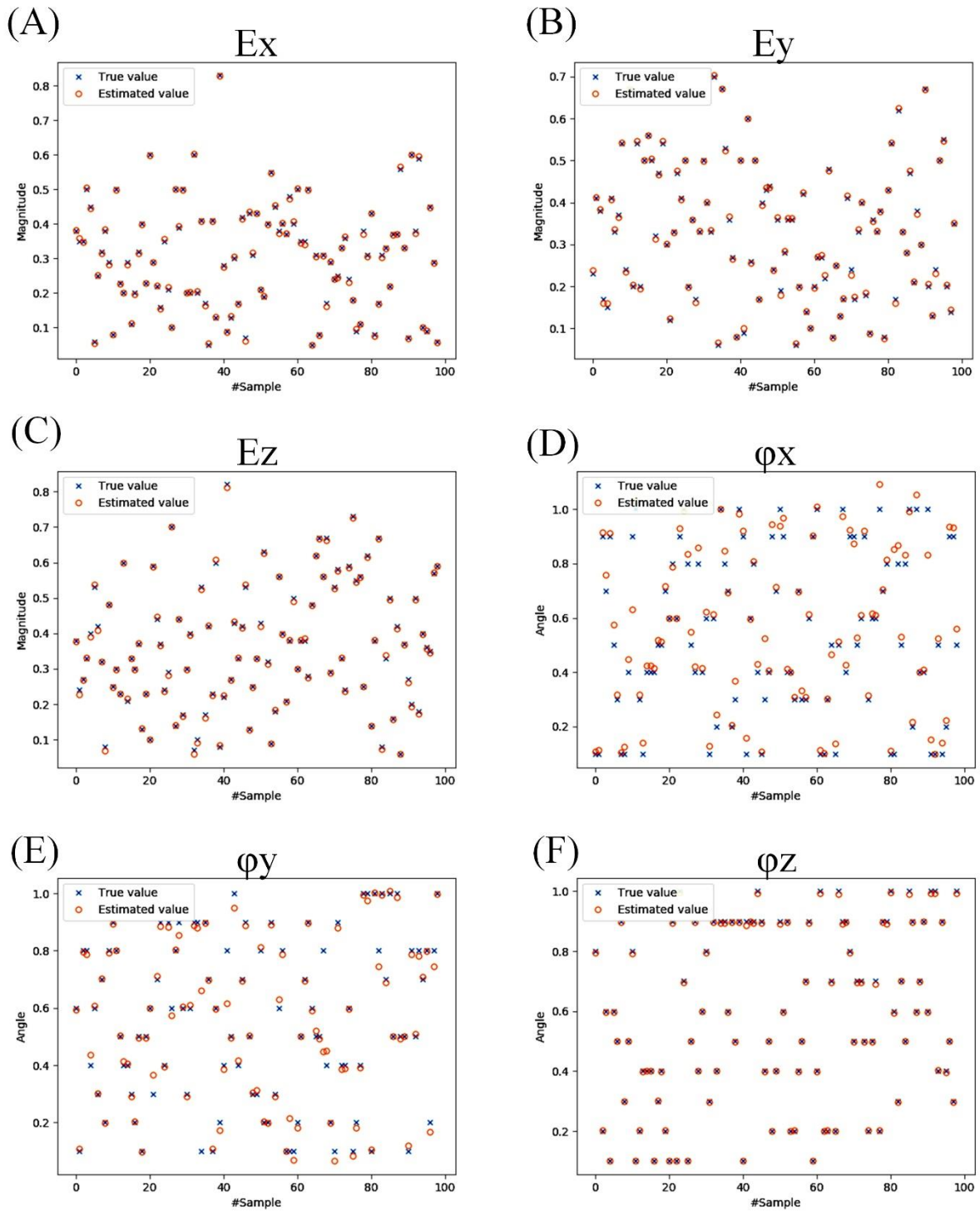

Fig. S4. The comparison of the MANN-predicted values of the six elements of 3D vectorial fields and the true values based on the test dataset.

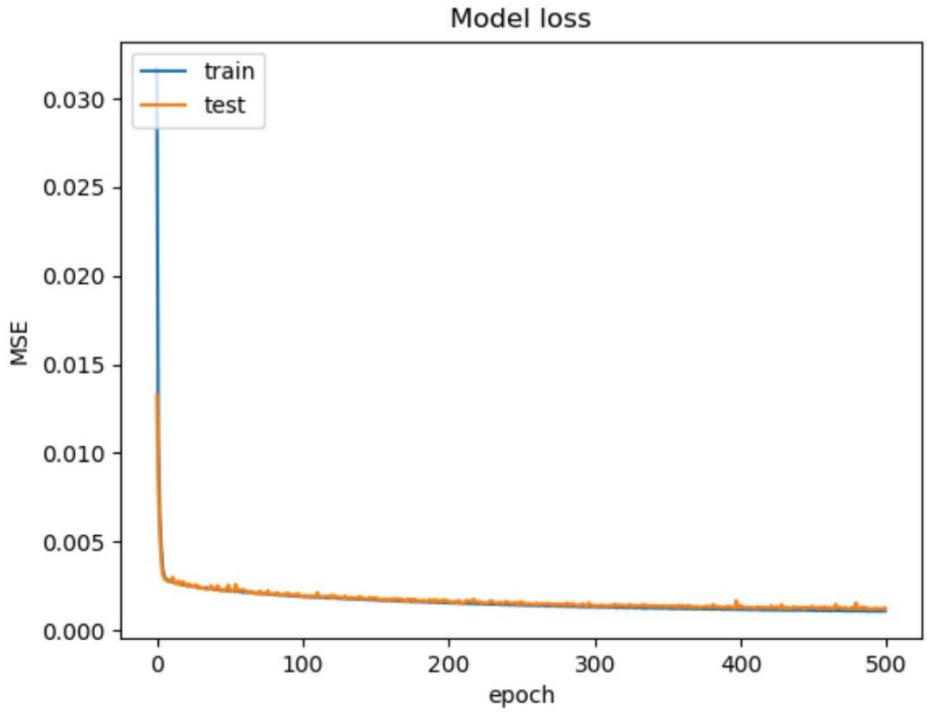

Fig. S5. Training loss of the MANN model. The model loss represented as the mean squared error (MSE) has sharp declines.

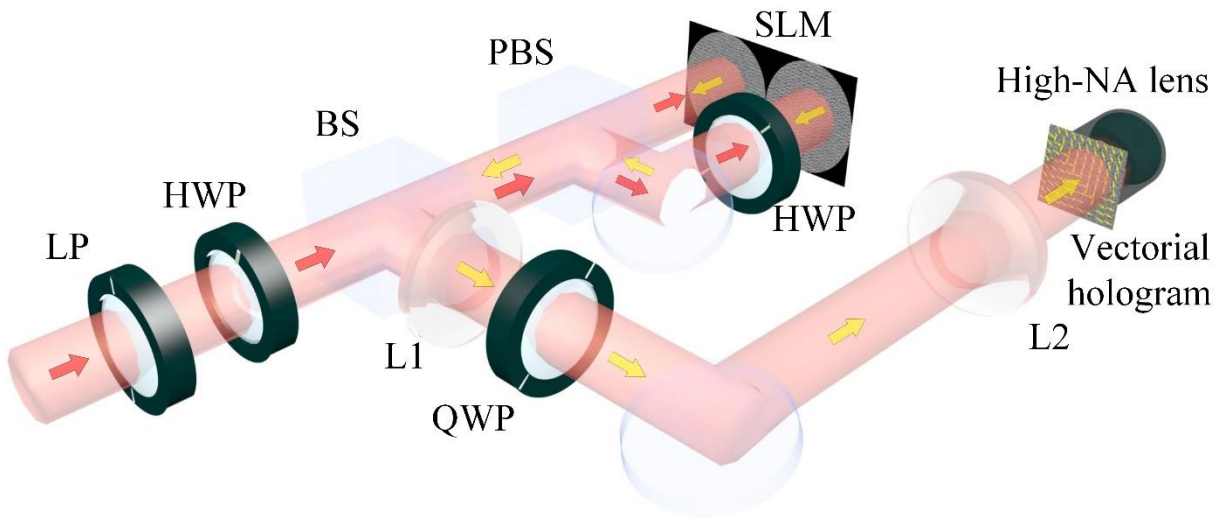

Fig. S6. Optical setup for the generation of a vectorial hologram for the reconstruction of a 3D vectorial holographic image based on a split-screen SLM. LP: linear polarizer, HWP: half wave plate, BS: beamsplitter, PBS: polarization beamsplitter, QWP: quarter wave plate, SLM: spatial light modulator, L1 and L2: optical lenses. The red and yellow arrows label out the propagation directions of the incident laser beam and the phase-modulated laser beam reflecting from a split-screen SLM, respectively.

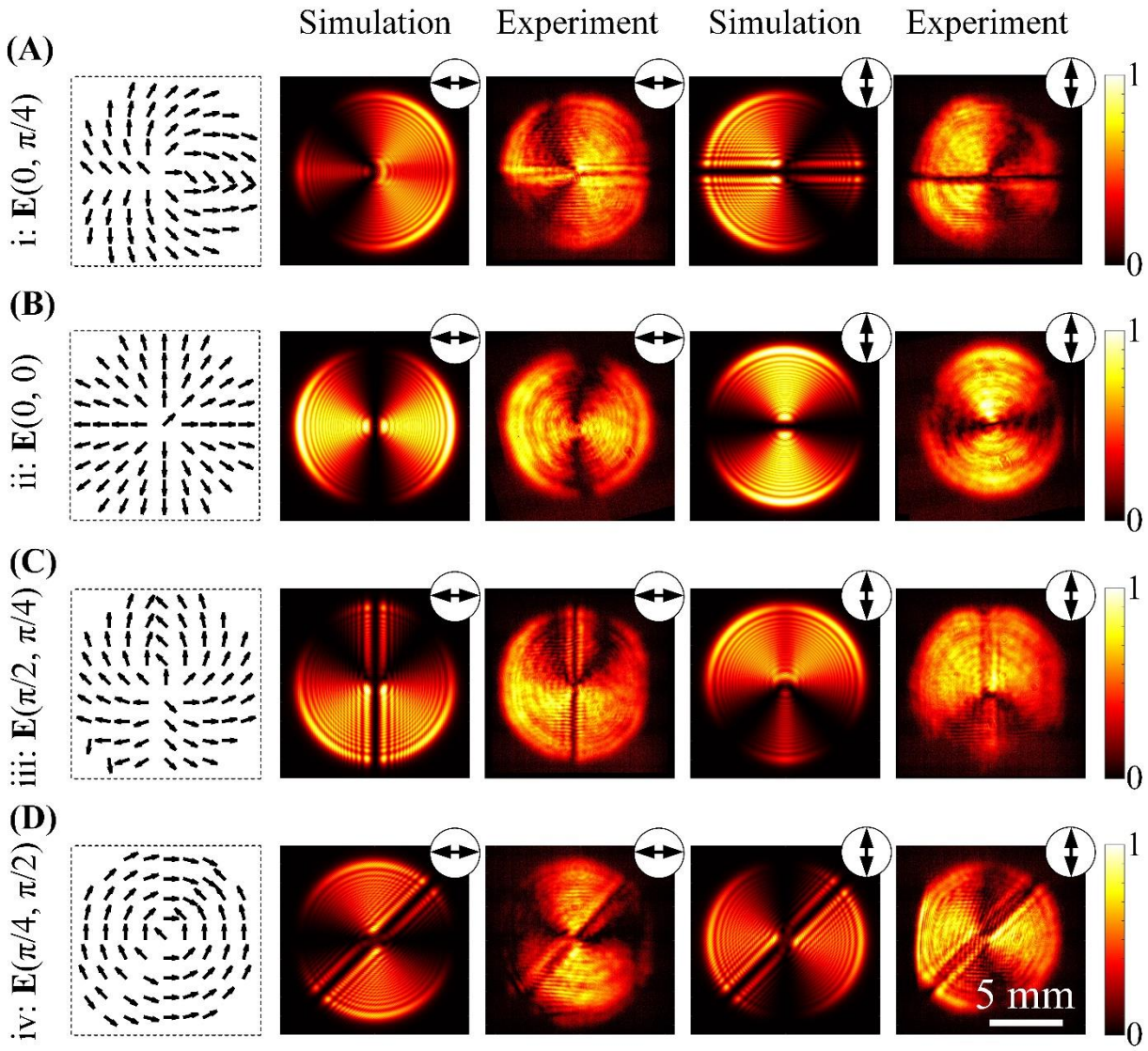

Fig. S7. The numerical simulation and experimental verification of the generation of four different 2D vector fields derived from the MANN.

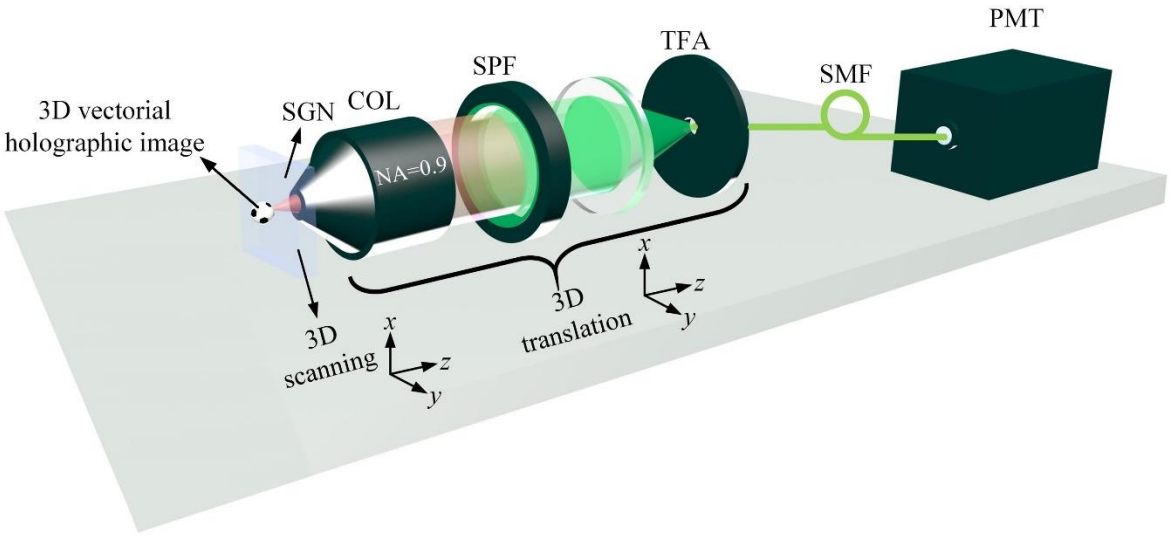

Fig. S8. Optical setup for the characterization of a vectorial holographic image through the fluorescence imaging of single gold nanorods. SGN: single gold nanorods, COL: collecting objective lens, SPF: short-pass filter, TFA: terminated fiber adapter, SMF: single-mode fiber, PMT: photomultiplier tube.

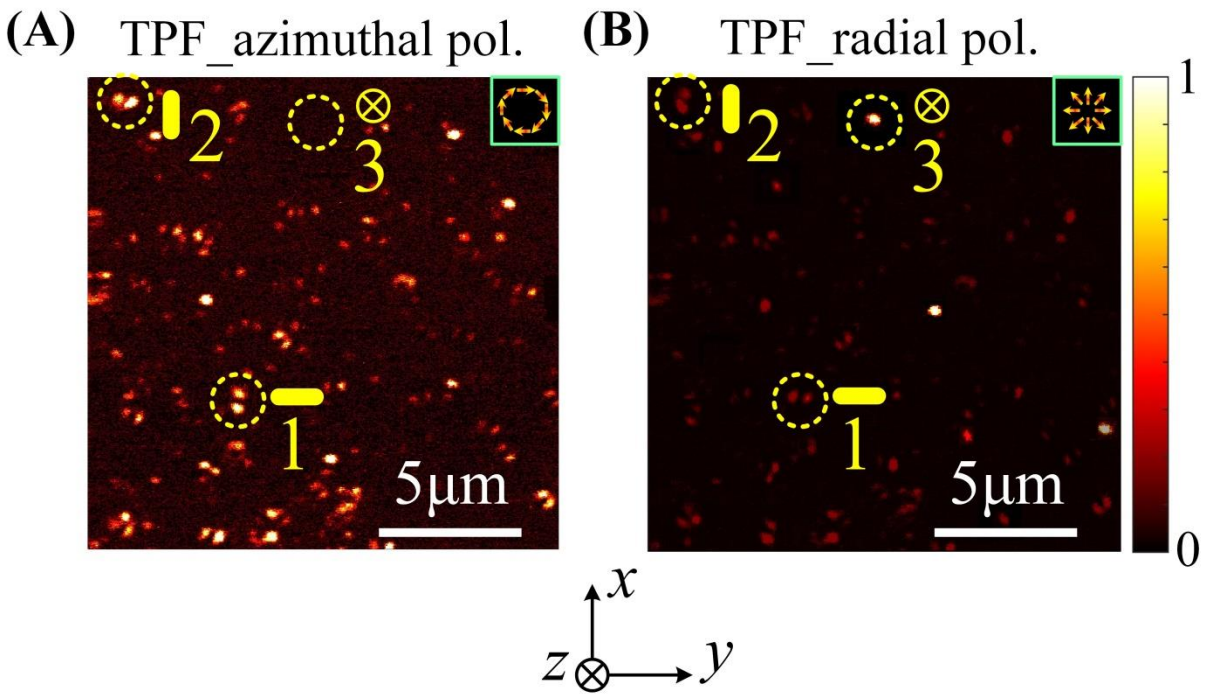

Fig. S9. Experimental characterization of the orientation of single gold nanorods through the polarization imaging using the azimuthal (A) and radial (B) polarization, respectively.

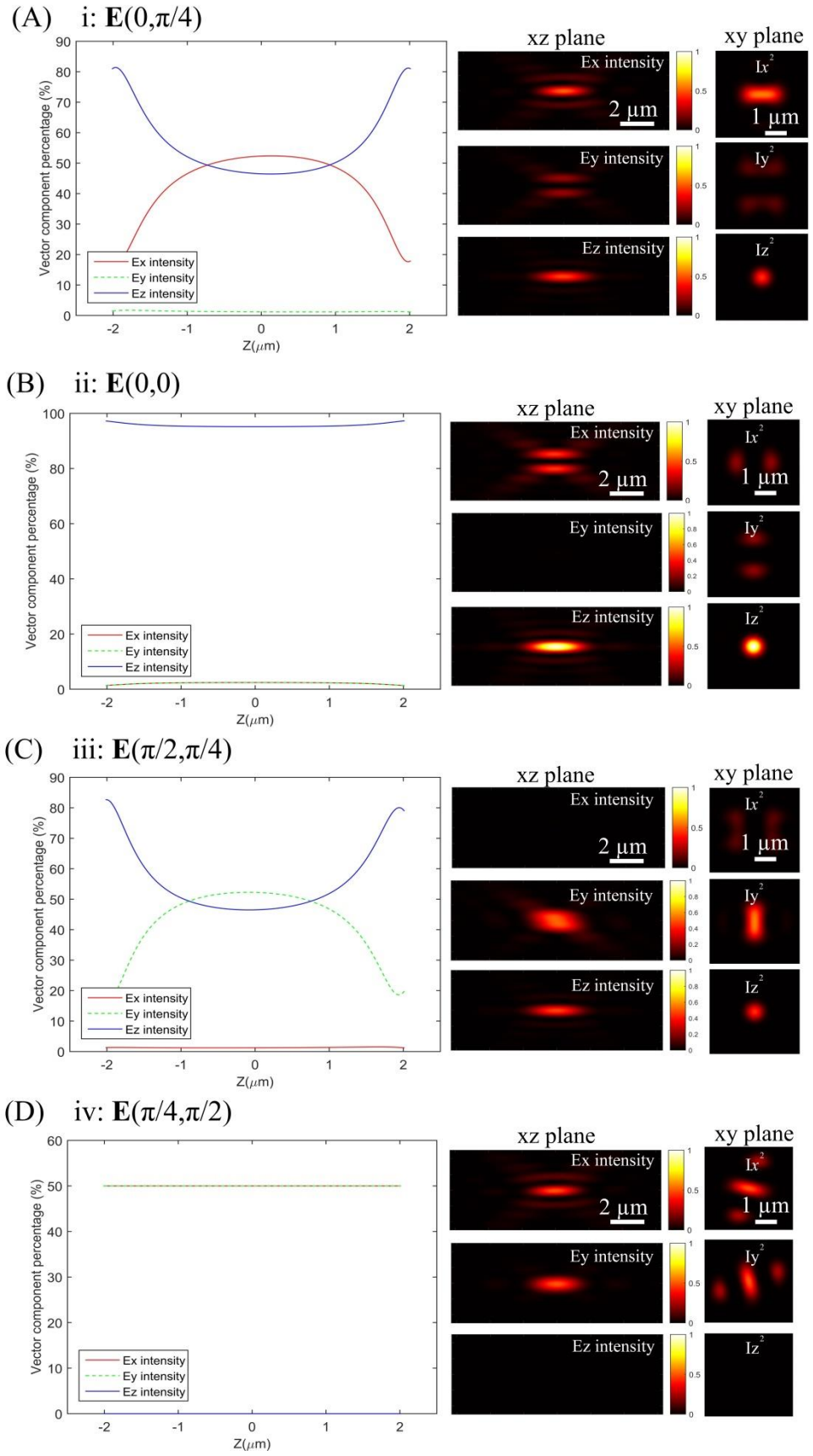

Fig. S10. Numerical characterization of four 3D vectorial fields of i: E(0, π/4) (A), ii: E(0, 0) (B), iii: E(π/2, π/4) (C), and iv: E(π/4, π/2) (D) in both transverse and longitudinal planes.

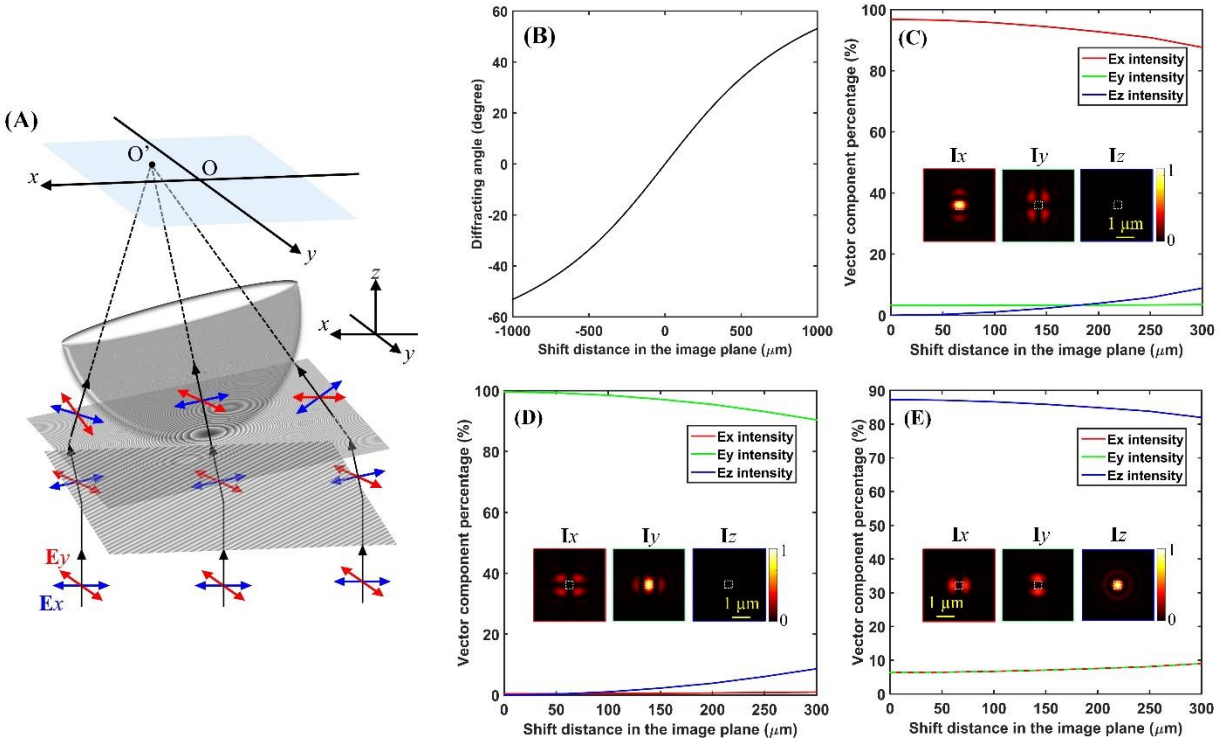

Fig. S11. Numerical characterization of the correlation between the azimuthal and radial spatial components and the three orthogonal components (E_x, E_y, E_z) for a large-angle diffracted optical beam. (A) The schematic of the reconstruction of a 3D vectorial field with a transverse shift in the image plane. (**B**) The numerically characterized deflection angle with respect to the spatial shift in the image plane. (**C-E**) The numerically simulated intensity distributions of the three orthogonal components in the image plane based on the incidence of the azimuthal and radial spatial components presented in Fig. 2B.

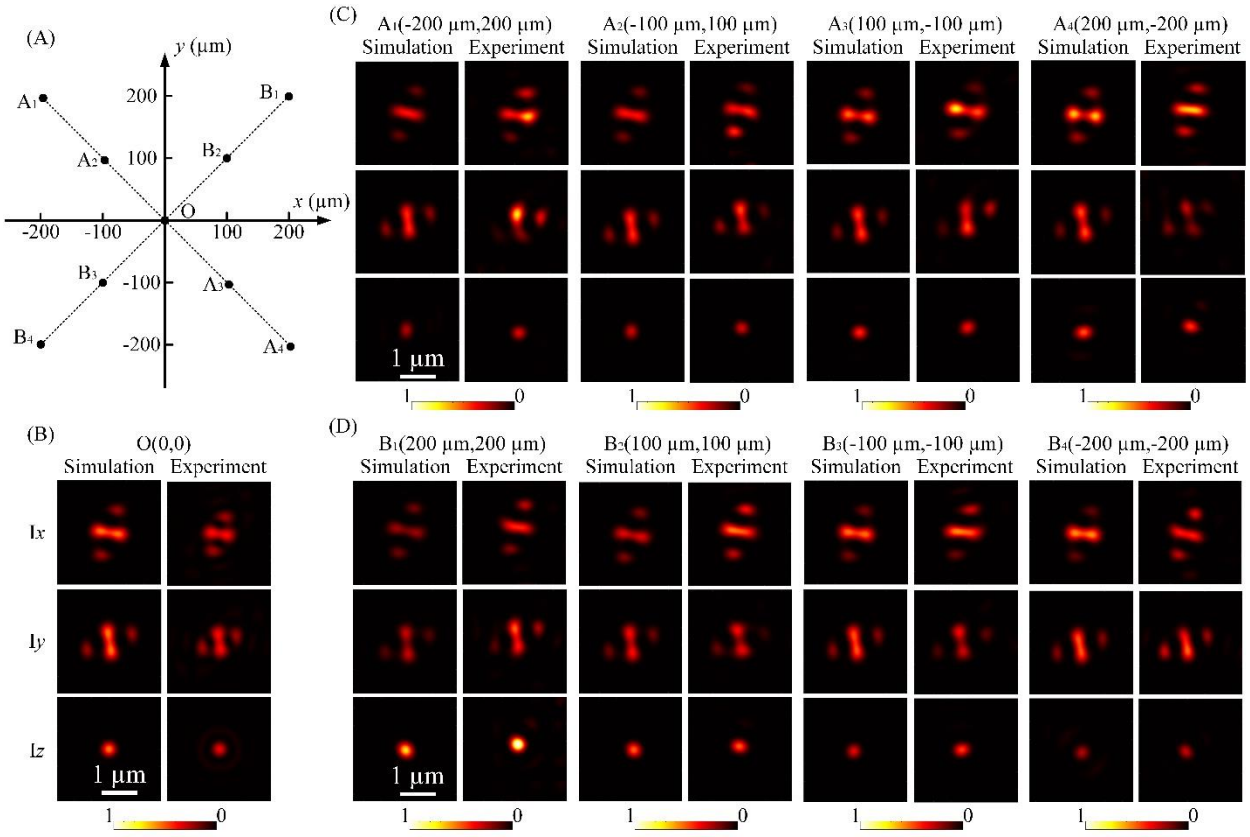

Fig. S12. The numerical and experimental characterization of a 3D vectorial field of E(π/4, π/4) at different transverse positions in the image plane. (**A**) Schematic of the characterization positions in the image plane. (**B**) The numerically and experimentally characterized intensity distributions of the three electric field components at the optical axis. (**C** and **D**) The numerically and experimentally characterized intensity distributions of the three electric field components at different positions in the image plane.

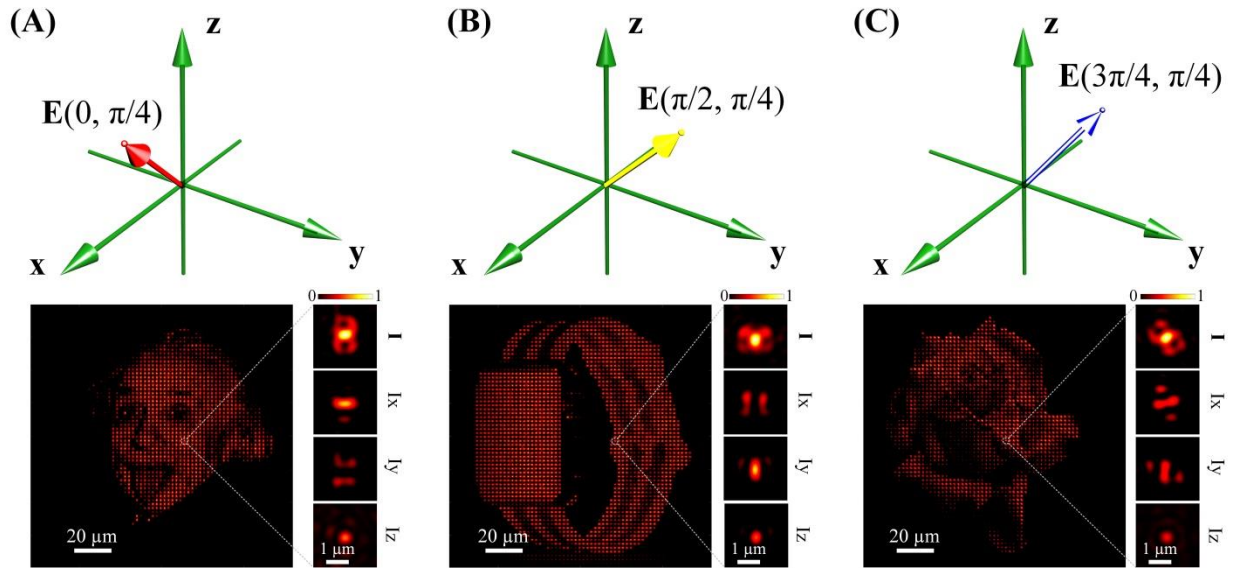

Fig. S13. Experimental characterization of 3D vectorial holographic images with three different 3D vectorial field distributions of E(0, π/4) (A), E(π/2, π/4) (B), and E(3π/4, π/4) (C), respectively, wherein random pixels were selected from the holographic images for the characterization of their 3D electric field components (insets).

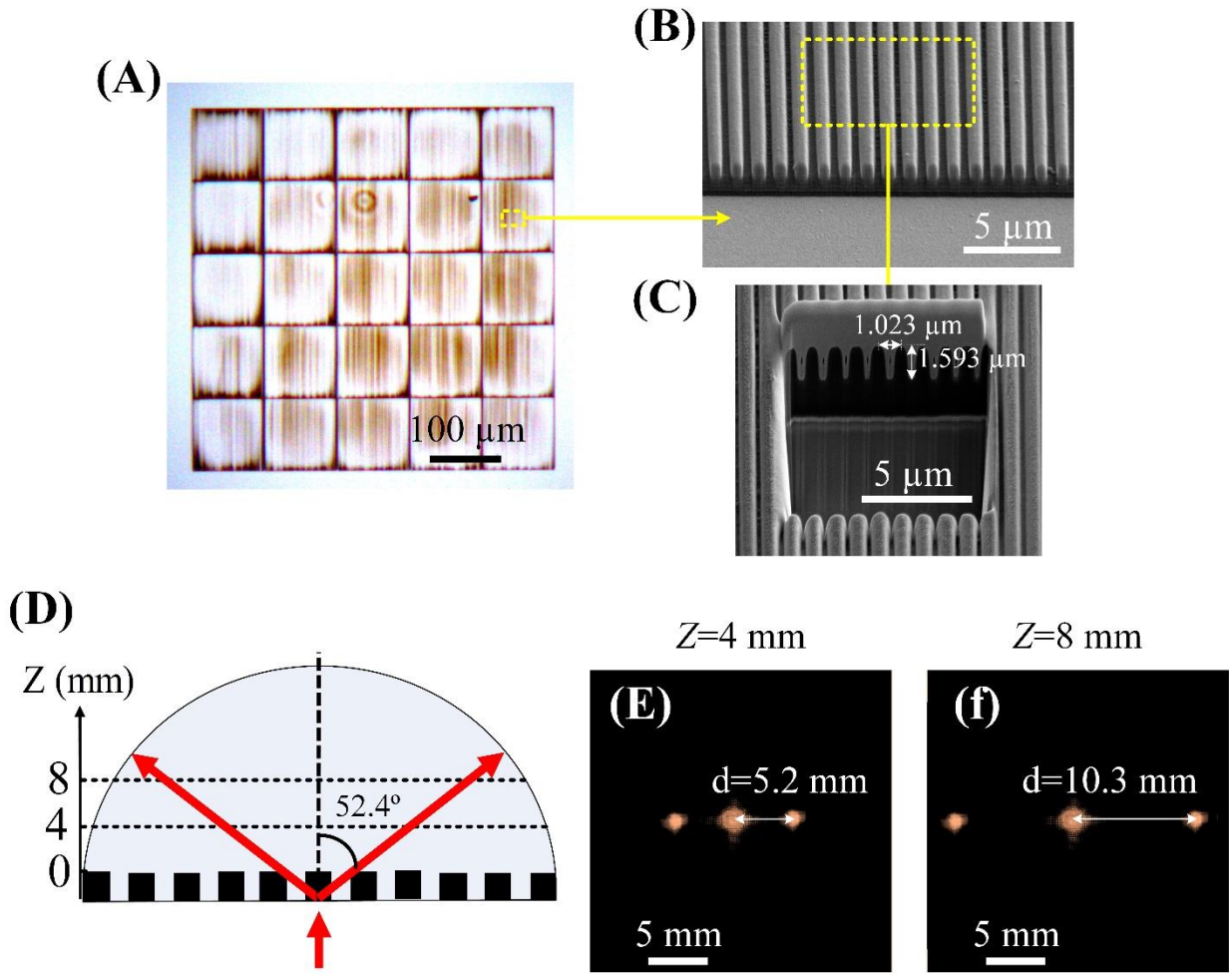

Fig. S14. Experimental characterization of the large beam deflection by a binary diffraction grating with a period of 1 *μm* at a wavelength of 808 *nm*. (**A**) Optical image of the laser-printed binary grating with a size of 1 *mm* by 1 *mm*. (**B**) The scanning electron microscopy (SEM) image of an enlarged area in (A). (**C**) The scanning electron microscopy image of a small area in the binary diffraction grating after being milled by the focused ion beam lithography, wherein the lateral resolution and the axis resolution were labelled out to validate the high-resolution 3D laser manufacturing. (**D**-**F**) The experimental characterization of the binary grating with a large-angle light deflection of 52.4 degrees at a wavelength of 808 *nm*.

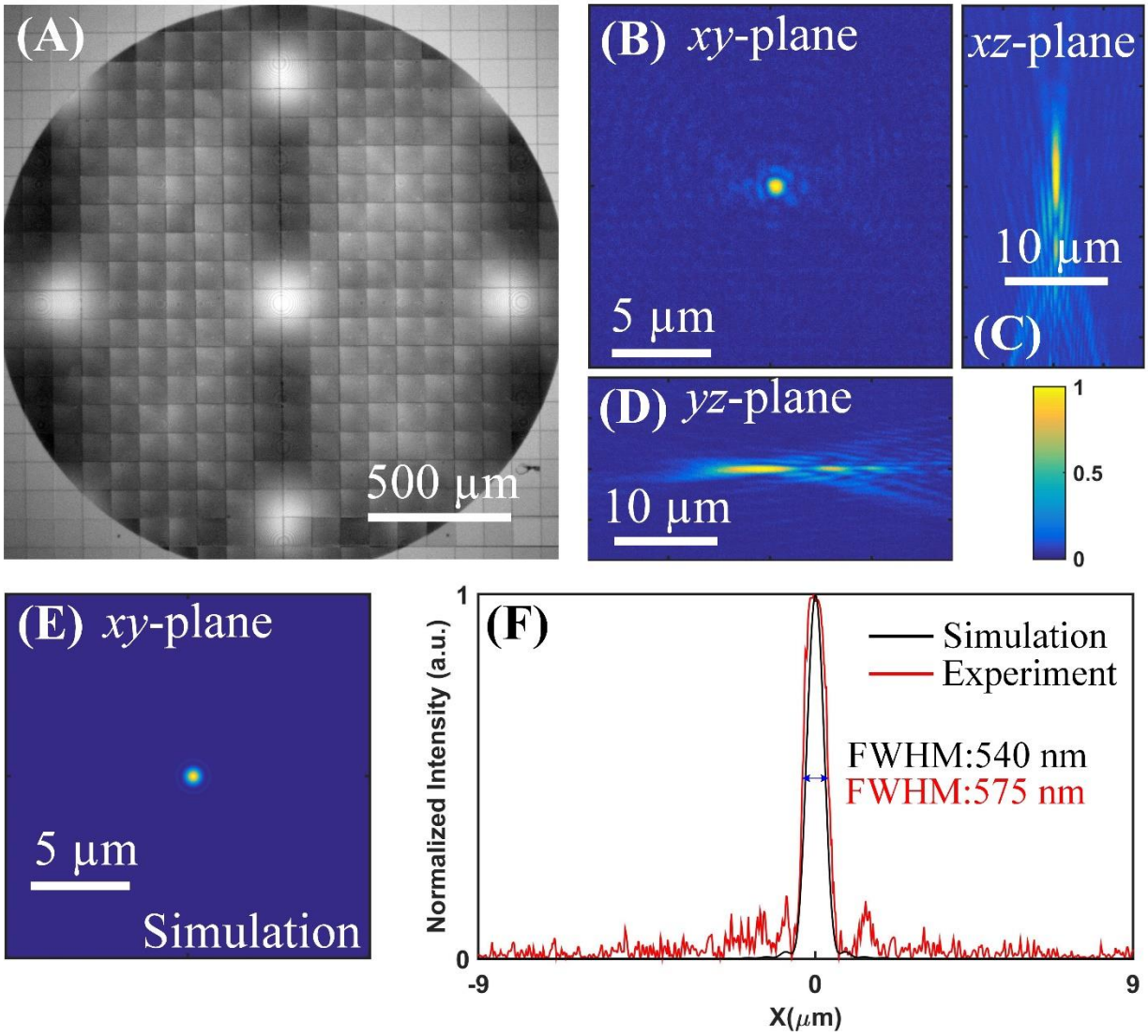

Fig. S15. Experimental characterization of a large-angle FT holographic lens capable of performing the diffraction-limited focusing. (**A**) Optical image of the laser-printed holographic lens. (**B**-**D**) Confocal images of the characterized intensity distribution of the focal field based on a plane wave incidence in the *xy*, *xz*, and *yz* plane of the focal region, respectively. (**E**) The simulated diffraction-limited focus in *xy* plane. (**F**) The comparison of the full width at half maximum between the experimentally characterized focal field and the simulated diffraction-limited focal field.

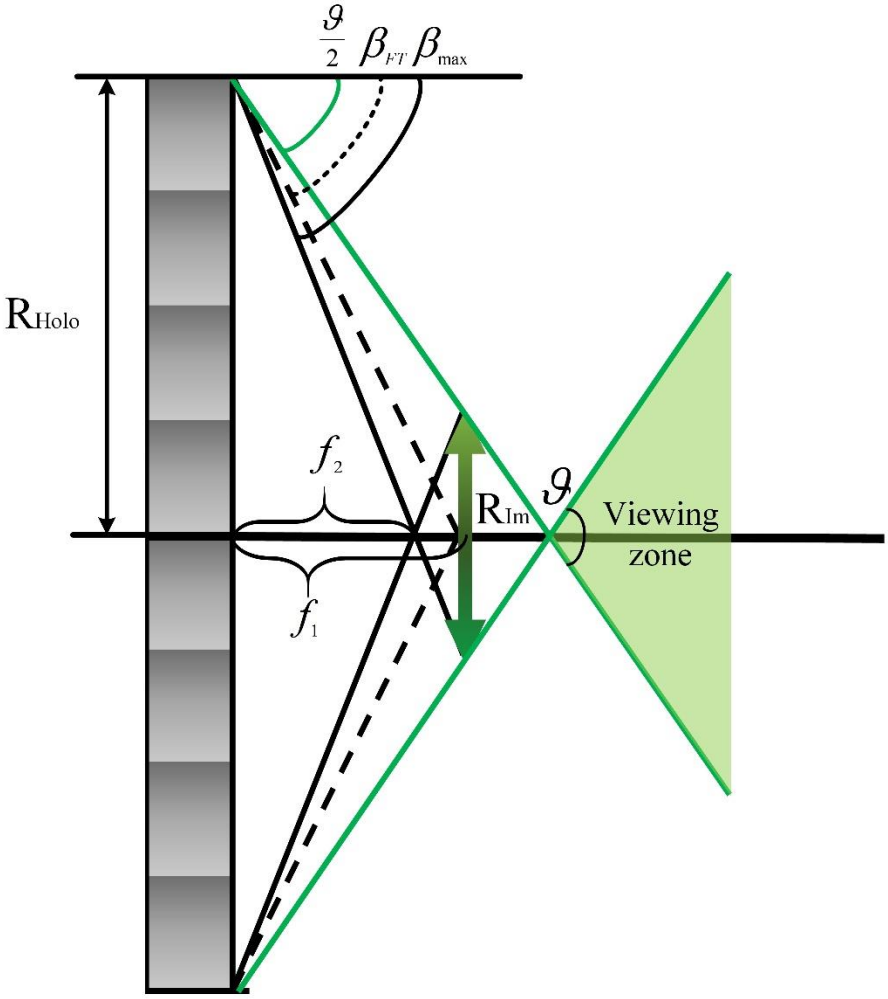

Fig. S16. Schematic illustration of the holographic image size, reconstruction distance, and the viewing angle of a vectorial hologram.

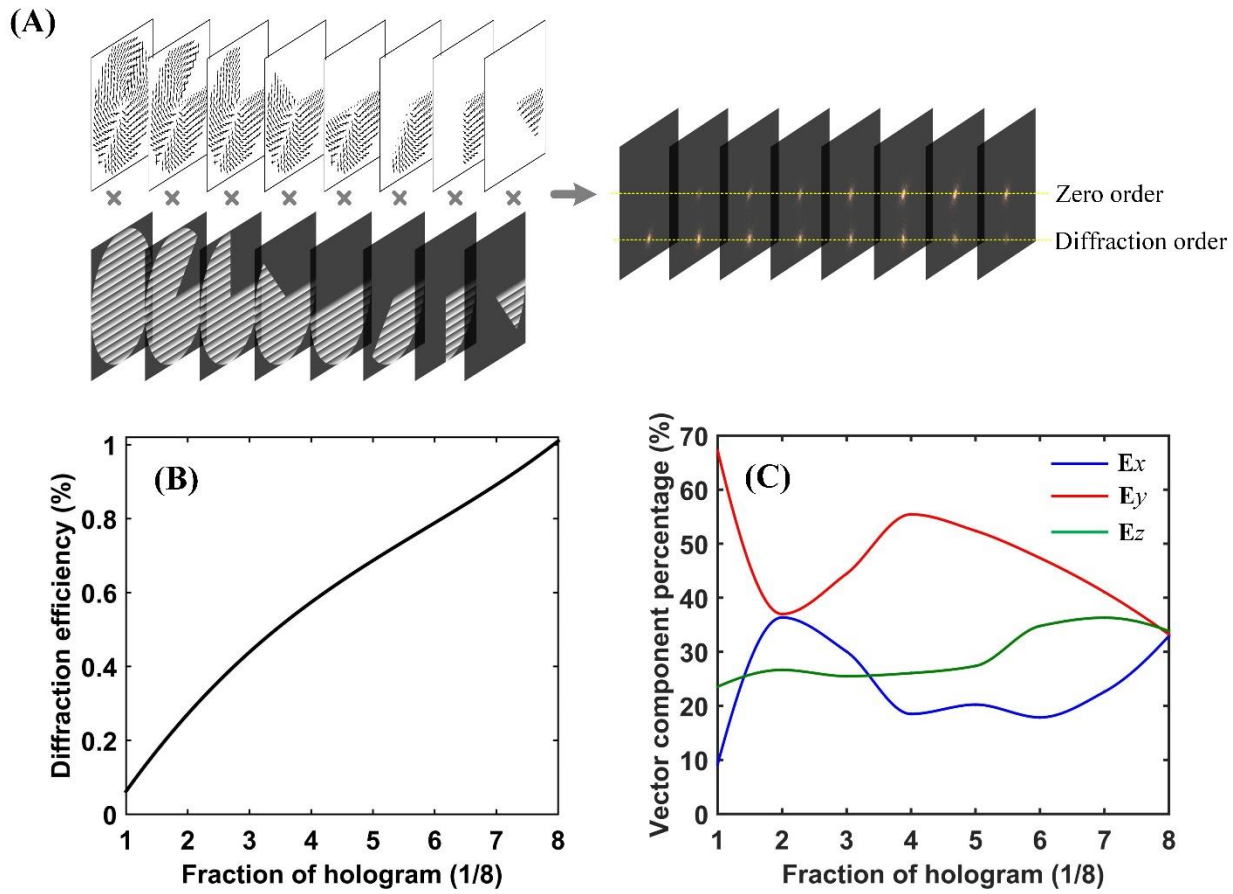

Fig. S17. The numerical characterization of the divisibility property of vectorial holograms. (**A**) Numerically simulated diffraction patterns by using different sections of a vectorial hologram consisting of a 2D vector field and a blazed grating. (**B** and **C**) The numerically characterize diffraction efficiency (B) and the 3D vector components percentage (C) for different fractions of a blazed grating, respectively.

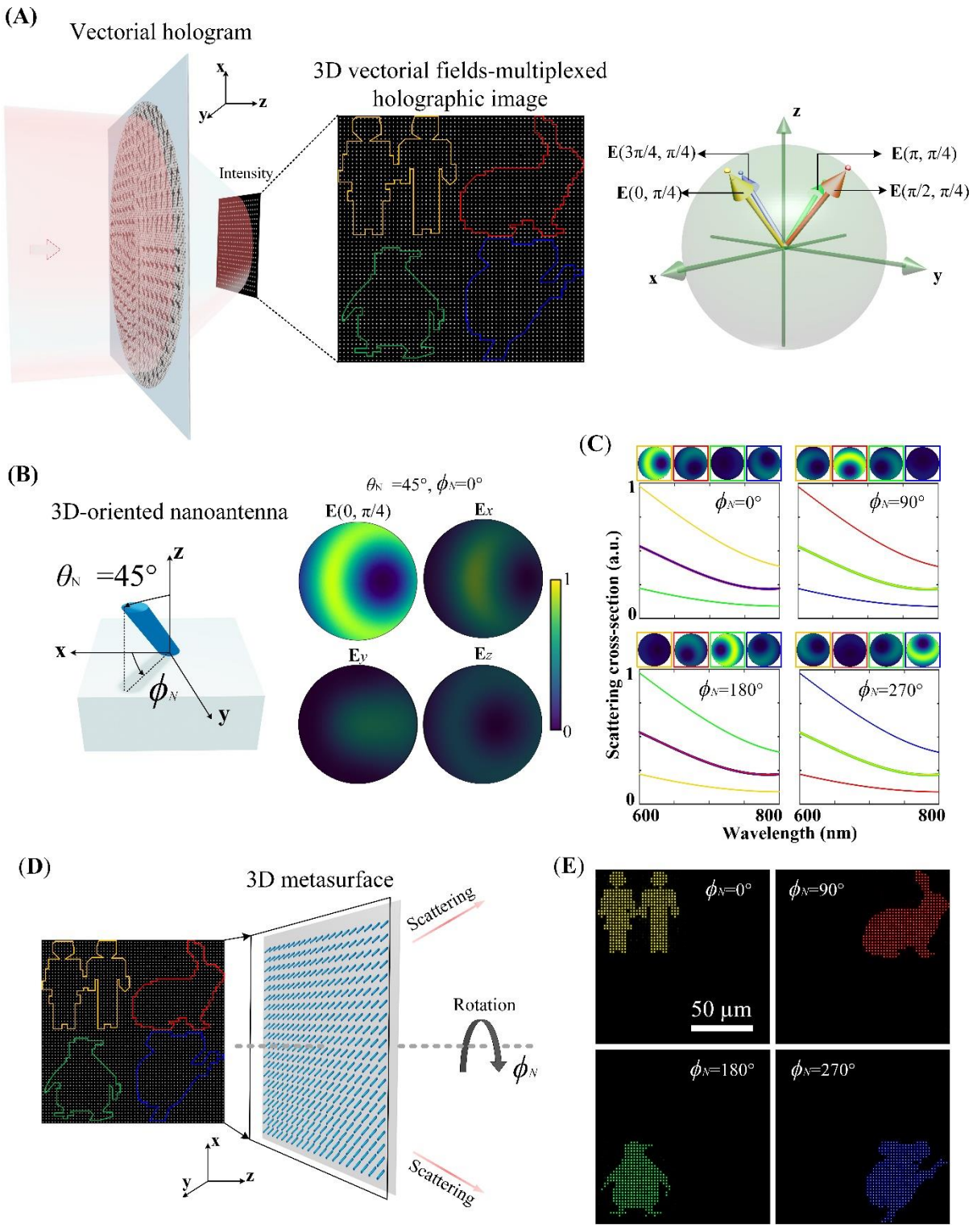

Fig. S18. Numerical characterization of the excitation of a 3D metasurface which consists of a 3D-oriented nano-antenna array through the generated 3D vectorial fields. (**A**) Schematic

illustration of the generation of a 3D vectorial fields-multiplexed holographic image, wherein pixels carrying four different 3D vectorial fields of **E**(0, π/4), **E**(π/4, π/4), **E**(π/2, π/4), and **E**(3π/4, π/4) are colour labelled by different contour lines on the intensity distribution of the holographic image. (**B**) Schematic of a 3D-oriented nano-antenna with a fixed polar angle of 45 degree. The right parts present back focal plane images of a 3D-oriented nano-antenna (polar angle θ_N=45º; azimuthal angle ϕ_N=0º) under the excitation of a 3D vectorial field of **E**(0, π/4), and linear polarization states along E_x, E_y, E_z, directions, respectively. (**C**) Scattering spectral and back focal plane images (top) of 3D-oriented nano-antennas with a fixed polar angle θ_N=45º and an azimuthal angle of ϕ_N=0º, 90º, 180º, and 270º, respectively, under the excitation of four different 3D vectorial fields of **E**(0, π/4), **E**(π/4, π/4), **E**(π/2, π/4), and **E**(3π/4, π/4), respectively. (**D**) Selective display of 3D vectorial fields-multiplexed optical information based on the rotation of a 3D metasurface consisting of a 3D-oriented nano-antenna array, wherein four 3D vectorial fields-encrypted images can be selectively scattered out by azimuthally rotating the 3D metasurface. (**E**) Numerically simulated far-field images of the four 3D vectorial fields-encrypted optical information based on the 3D metasurface with an azimuthal orientation of ϕ_N=0º, 90º, 180º, and 270º, respectively.

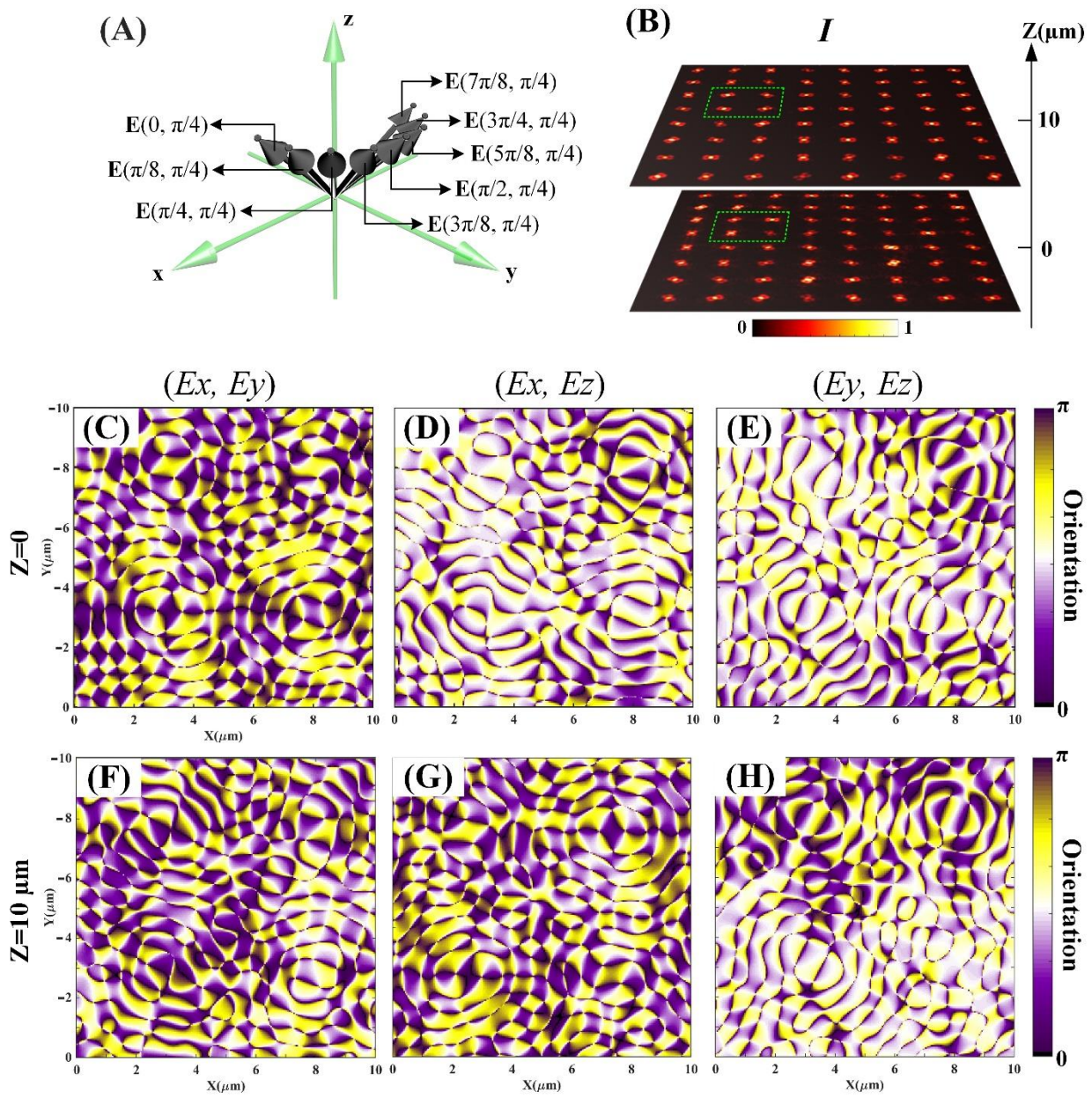

Fig. S19. The numerically simulated random multiplexing of 3D vectorial fields in a holographic image, leading to an array of 3D vectorial vortices/singularities. (**A**) Schematic of eight different 3D vectorial fields used for the holographic multiplexing. (**B**) The simulation result of random 3D vectorial field distributions in a 3D holographic image by using the eight 3D vectorial fields in (A). (**C** to **H**) The 3D vectorial vortices/singularities in the electric field components of (E_x, E_y), (E_x, E_z), and (E_y, E_z) in the z=0 and z=10 μm image plane, respectively.